Soft Matter

PAPER

View Article Online
View Journal | View Issue

Cite this: *Soft Matter*, 2018, **14**, 8509

Suction effects of craters under water†

Shutao Qiao,‡[a] Liu Wang,‡[a] Kyoung-Ho Ha[b] and Nanshu Lu*[abcd]

Received 4th August 2018,
Accepted 10th October 2018

DOI: 10.1039/c8sm01601a

rsc.li/soft-matter-journal

Octopus-inspired cratered surfaces have recently emerged as a new class of reusable physical adhesives. Preload-dependent adhesion and enhanced adhesion under water distinguish them from the well-studied gecko-inspired pillared surfaces. Despite growing experimental evidence, modeling frameworks and mechanistic understanding of cratered surfaces are still very limited. We recently developed a framework to evaluate suction forces produced by isolated craters in air. In this paper, we focus on underwater craters. The suction force–preload relation predicted by this framework has been validated by experiments carried out with an incompressible fluid under small and moderate preloads. Our model breaks down under a large preload due to multiple possible reasons including liquid vaporization. A direct comparison between liquid and air-filled craters has been carried out and the dependence on the depth of water has been revealed. We find that the suction forces generated by underwater craters scale with the specimen modulus but exhibit non-monotonic dependence on the aspect ratio of the craters.

1. Introduction

Adhesives that can stick and unstick repeatedly are called reversible or reusable adhesives. Reversible adhesives can find many applications such as in wall mounts, foot pads for robots,[1,2] wafer handlers,[3–6] and bio-integrated electronics.[7,8] Desirable properties of reversible adhesives include fast and clean removal, tunable adhesion, and reliable attachment under both dry and wet conditions. Although permanent wet or underwater adhesives have undergone fast development,[9,10] strong but reversible underwater physical adhesives still remain challenging.[11]

Full of microfibrils, gecko toe pads are found to be remarkable physical adhesives. Their adhesion strength was measured to be 100 kPa,[12,13] comparable to that of 3M scotch tapes (200 kPa). It has been revealed that the adhesion of microfibrils comes from van der Waals interactions.[14,15] Contact mechanics has been applied to explain the enhanced adhesion when the fibril diameters decrease.[16] Extensive efforts have been made to produce gecko-mimetic artificial microfibrils[17–19] and micro-spatula[20] as reusable adhesives. However, their adhesion strength is fixed once fabricated unless extra engineering is incorporated.[21–23] It's also reported that wet surfaces or underwater environments impair the performance of microfibril-enabled adhesives.[24–26] Therefore, alternative mechanisms are required for reversible adhesives with tunable adhesion in air and under water.

The inspiration for reversible underwater adhesion comes from aquatic cephalopods such as squids and octopuses whose arms are equipped with hundreds of suckers.[27–30] For example, octopuses can easily anchor onto different terrains and substrates by actively manipulating muscles on their tentacles. Such an attachment is enabled by the suction force due to the pressure difference between the sucker and the ambient, termed negative pressure, which can roar up to 300 kPa for octopuses and 800 kPa for decapods under water.[31,32] The fact that microfibrils are found on the toe pads of lizards and insects while suckers evolved for marine animals implies that suction is more effective than van der Waals interactions under water.

In fact, it is also our everyday experience that macroscopic suction cups are effective in attachment. Several papers have already modeled thin-walled suction cups.[33–35] But macroscopic single suction cups are not flexible enough to conform to complex three-dimensional surfaces. While microscale suction cups have been built at the tip of micro-pillars,[36–39] the effect of van der Waals force *versus* suction force is still under debate.[38,40,41] Moreover, slender micro-pillars suffer from notorious issues such as mechanical integrity after repetitive use.[42–45] As a result, in recent years, arrays of micro-craters emerged as a novel surface texture for reversible adhesion due

[a] *Center for Mechanics of Solids, Structures and Materials, Department of Aerospace Engineering and Engineering Mechanics, the University of Texas at Austin, 210 E. 24th St, Austin, TX 78712, USA. E-mail: nanshulu@utexas.edu; Tel: +1512-471-4208*
[b] *Department of Mechanical Engineering, the University of Texas at Austin, 210 E. 24th St, Austin, TX 78712, USA*
[c] *Department of Biomedical Engineering, the University of Texas at Austin, 210 E. 24th St, Austin, TX 78712, USA*
[d] *Texas Materials Institute, the University of Texas at Austin, 210 E. 24th St, Austin, TX 78712, USA*

† Electronic supplementary information (ESI) available. See DOI: 10.1039/c8sm01601a

‡ These authors contributed equally to this work.

to ease of fabrication, high conformability to curvilinear surfaces, and reusability. For example, in 2014, closely packed sub-micron-sized surface dimples on UV resin were reported with shear adhesive strength of 750 kPa under a preload of 3 N[4], which is very competitive among gecko-inspired dry adhesives.[46] In 2015, Choi *et al.* fabricated 1 μm-diameter craters on the surface of polydimethylsiloxane (PDMS) and measured the shear adhesive strength to be 1.6 kPa, higher than that of the same PDMS with both flat surface or pillars on the surface.[7] In 2016, surface craters covered with a layer of thermoresponsive hydrogel demonstrated switchable adhesion by heat, and was applied for transfer printing of semiconducting nanomembranes.[5] In 2017, arrays of octopus-inspired micro-craters with a built-in protuberance structure demonstrated load-dependent adhesion under both dry and wet conditions,[47] distinct from that of gecko-like adhesives. Most recently, Baik *et al.* reported that micro-pillars with concave tip geometry exhibit high dry/wet adhesion against both a smooth surface and rough, hairy skin.[39] Even when applied on irregular surfaces, nanosucker arrays of flexible polydimethylsiloxane (PDMS) have generated strong adhesion.[6]

Despite the fact that many papers have attributed the strong attachment of cratered surfaces to suction effects,[5,47–49] there is a lack of comprehensive mechanistic understanding of the suction generation process, not to mention the governing parameters. To date, only Baik *et al.*[47] have presented a closed-form solution for the adhesion strength of cratered surfaces. However, this analysis is flawed as it is based on the prior work of Afferrante *et al.*[33] and Tramacere *et al.*,[50] which is only applicable to thin-walled suction cups rather than craters. It is worth pointing out that craters are rather different from adhesives with microfluidic channels[51] as craters are dimples on the surface which are surrounded by thick walls formed by the polymer matrix. In our recent study,[52] we established the first theoretical framework to analyze isolated craters in air, obtained nonlinear solutions to preload-dependent suction forces, and validated our solutions by experiments. We have also unveiled the elasto-capillary effects on suction forces for miniature craters on soft polymers.[53] At this stage, to the best knowledge of the authors, no correct mechanistic understanding of underwater craters has been established. Such an understanding is critical to the design and the prediction of cratered surfaces working under wet conditions. Building upon our established framework and experimental skills for dry craters, herein we present a systematic study on the adhesion mechanism of an isolated crater under water. Our approach involves experimental, numerical, and analytical characterizations of isolated macroscopic craters for which size effects associated with surface phenomena are negligible. We focus on spherical-cap-shaped (SCS) craters, establish the suction-geometry, suction-preload, and suction-depth-of-water dependence, and identify the limitation of our analysis by comparing with experimental results. When we compare the suction effects of craters under both dry and wet conditions, we discover that the suction forces generated by underwater craters can be significantly larger than dry craters of the same shape and material, which explains the fact that most creatures utilizing suction for attachment are sea-lives.

This paper is organized as follows. In Section 2, we investigate the suction force produced by isolated hemi-spherical craters. We study such craters based on experimental, numerical simulation, and analytical approaches. After confirming the validity of our model, we then adopt the modeling framework for characterizing more general SCS craters. In Section 3, we calculate the suction forces of SCS craters of different shapes and at different preloads and compare them with experimental measurements, through which we identify the applicability of our model. In Section 4, we provide a brief summary of our key findings.

2. Hemi-spherical craters

In this section, we use experimental, computational, and analytical approaches to study isolated hemi-spherical craters under water. The computational framework established in this section will be applicable to more general classes of isolated craters.

2.1 Problem description

Consider a specimen containing a hemi-spherical crater with radius a at its bottom (Fig. 1a). The specimen rests on a fixed rigid platform, both submerged in a liquid. The liquid inside the crater is the same as in the ambient, and is characterized by the initial volume V_0, the total number of molecules N_0, and the hydrostatic pressure p_0 which can be written as

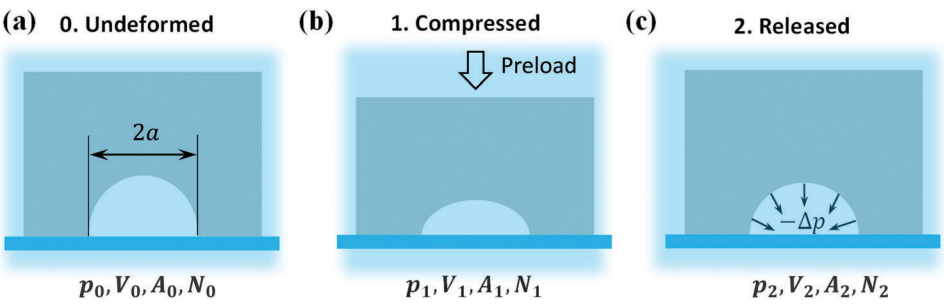

Fig. 1 Schematics for the loading–unloading cycle that produces a suction force under water: (a) a specimen with an isolated hemi-spherical crater of radius a resting on the flat bottom of a tank filled with liquid (blue); (b) the specimen is preloaded in compression and the liquid is squeezed out of the crater; (c) the preload is released, and the crater springs back, resulting in a pressure drop in the crater. The symbols p, V, A and N denote the pressure, volume, projected area, and number of liquid molecules inside the crater at each state.

$$p_0 = p_a + wh$$

where p_a is the atmospheric pressure, w is the specific weight of the liquid, and h is the distance from the cratered surface to the liquid surface, a.k.a. liquid depth. The projected area of the undeformed crater is denoted by A_0.

Under such settings, the suction effect can be realized in the following two sequential stages:

(1) The specimen is compressed, so that some liquid is squeezed out of the crater; at the end of this stage, the remaining liquid in the crater is characterized by the triplet (p_1, V_1, N_1) (Fig. 1b).

(2) The specimen is unloaded, so that the crater springs back partially. The elastic recovery of the specimen reduces the pressure of the liquid inside the crater, generating the suction effect. At the end of this stage, the liquid in the crater is characterized by the triplet (p_2, N_2, V_2) (Fig. 1c). Accordingly, the negative pressure generated is $\Delta p = p_2 - p_0$.

We are interested in the suction force upon full unloading which is defined as

$$F = -\Delta p A_2 \quad (1)$$

where A_2 is the projected area of the crater at the end of Stage 2. A complete analysis of the two-stage process requires one to model the liquid flow. In this paper, we avoid this task by adopting the following assumptions:

(1) The liquid flows freely out of the crater upon loading, so that $p_1 = p_0$.

(2) No liquid exchange takes place upon unloading, so that $N_1 = N_2$.

(3) The entire process is isothermal and the liquid is incompressible, so that $V_1 = V_2$.

The first assumption that the liquid can flow out freely when compressed is inspired by prior works on thin-walled suction cups.[33–35] In these models,[33–35] the analytical relationship between preload and suction-cup deformation has been obtained by neglecting gas or liquid resistance during compression. As for the second assumption that there is no leakage during unloading, it is consistent with experimental observations for thin-walled suction cups[33–35] as well as surface craters.[47] The third assumption of incompressible fluid is widely adopted for many liquids. With these three assumptions, the dynamics of liquid flow is regarded as a sequence of static equilibrium states. Consequently, it becomes sufficient to analyze the two-stage process in the context of solid mechanics, as explained in Section 2.3.

One must be aware that our first assumption is only valid when there is a finite amount of liquid left inside the crater at Stage 1. When the crater is fully closed, *i.e.* when all the liquid is squeezed out of the crater, complete vacuum is achieved inside the crater. As a result, the negative pressure is simply $-\Delta p = p_a + wh$, and will be maintained throughout the unloading process (Stage 2) if no backflow is allowed. The third assumption would break down once there is significant vaporization inside the crater, which occurs when the liquid pressure drops close to the saturated vapor pressure of this liquid. These extreme situations are elusive in the current model but we will offer in-depth discussions for them in Section 2.4.

In the remainder of Section 2, we describe an experimental setup designed to conform to the adopted assumptions and measure the suction force. Further, we show that the experimental results can be predicted using nonlinear elasticity theory up to moderate deformation. That means neglecting the dynamics of liquid flow appears to be a good assumption. In contrast, linear elasticity theory fails to predict the suction force under, important for practical purposes, moderate preloads.

2.2 Experiments

The experimental setup was designed so that it realized the two-stage process under conditions that well represent the adopted assumptions. First, polydimethylsiloxane (PDMS, Sylgard 184 Dow Corning) with the base-to-curing-agent mass ratio equal to 30 : 1 was cured at 70 °C for 12 hours to mold a cylindrical specimen with diameter 25.40 mm and height 35.13 mm. A hemi-spherical crater of diameter 12.70 mm was placed at the center of a circular face. The material constitutive behavior was measured to fit an incompressible neo-Hookean model with shear modulus $\mu = 47.3$ kPa in our recent work.[52] Note that a hydrostatic pressure will not induce any deformation in an incompressible polymer.[54] During the entire loading–unloading process (Fig. 1), as long as there is still incompressible fluid inside the crater, the whole specimen would be subjected to a hydrostatic pressure $p_0 = p_a + wh$. On top of that, a negative pressure is applied inside the crater during the unloading stage. Superimposing an imaginary hydrostatic tensile stress $\sigma = wh$ onto the whole specimen changes its hydrostatic stress state to $p_0 - \sigma = p_a$, yet introducing no deformation due to its incompressibility. In other words, the specimens' response is independent of the liquid depth h, yielding a depth-independent suction effect. However, this argument breaks down when the incompressibility of the filling liquid no longer holds. For example, when the liquid is fully squeezed out at the end of Stage 1 or when the liquid starts to vaporize. Both situations will be discussed in detail in Section 2.4. Neglecting the two extreme cases at this point, we can simply fill the crater with incompressible fluid and perform the experiments in air at sea level, *i.e.*, $h = 0$ and $p_0 = p_a$ in our experiment.

To realize experimental conditions that well represent the adopted assumptions, we built a special platform as illustrated by the schematic in Fig. 2a. The corresponding photograph is offered in Fig. 2b. The cratered specimen was compressed against a stiff acrylic platform. At the center of the platform, we drilled a ventilation hole with a diameter of 0.8 mm, which was used for releasing and trapping liquid in the crater. During Stage 1 (loading), consistent with the first assumption, the vent hole was kept open. During Stage 2 (unloading), consistent with the second assumption, the hole was sealed. Without the vent hole, we noticed that there was resistance against liquid flowing out. Therefore, future studies should be carried out accounting for such resistance.

Direct measurements of the suction force upon unloading are difficult. Therefore we performed the loading–unloading–pulling-off

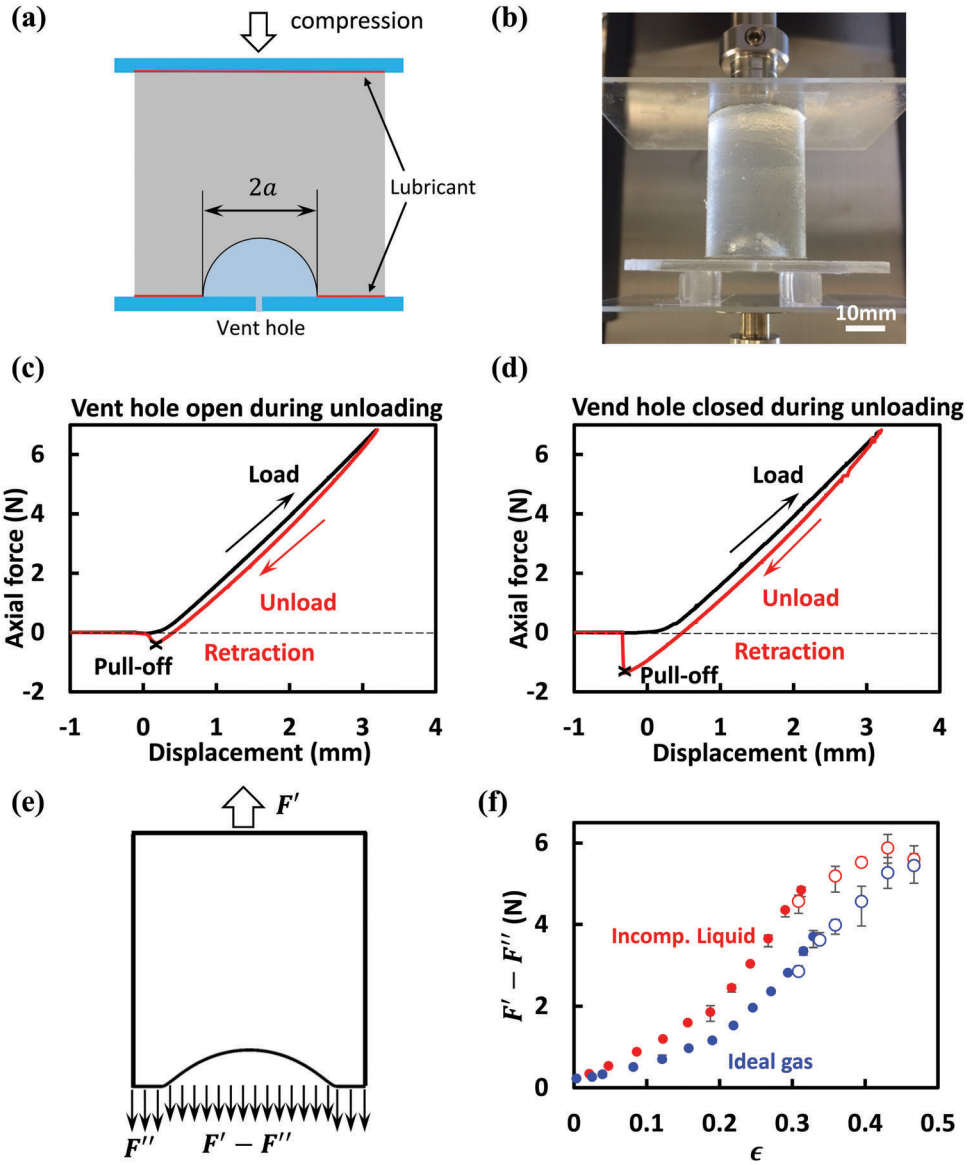

Fig. 2 A schematic (a) and a photograph (b) of the experimental setup. The small ventilation hole drilled in the bottom platform is open during loading and closed during unloading. Load–displacement curves with vent hole open (c) and closed (d) during unloading. Peak compressive strain was 10%. Loading, unloading, retraction stages, and the pull-off points are identified. (e) A schematic of the free body diagram of a specimen at pull-off. (f) Comparisons of experimentally measured suction forces ($F' - F''$) of air-filled (blue markers) and liquid-filled (red markers) craters. Data obtained by DMA are represented by solid dots and MTS by hollow circles.

experiments on the specimens and measured the pull-off force rather than the suction force. These data will be used to extract the suction force. We conducted a series of uniaxial compression and retraction tests using a Dynamic Mechanical Analyzer (DMA) (RSA-G2, TA Instruments) and a Mechanical Testing System (MTS Servohydraulic load frame with Instron 8500R controller). The load cell of the DMA has good resolution (10 μN) but limited range (up to 35 N), whereas the load cell in the MTS (Omega LCHD-50) has sufficient range (222 N) but lower resolution (0.22 N). Thus, experiments with loading forces greater than 35 N were performed with the MTS, while the rest were done using the DMA. In both testing systems, the top and bottom surfaces of the specimen were lubricated by performance oil (Fellowes Powershred Performance Shredder Oil) such that the specimen was free of friction and loaded under uniaxial stress. The loading velocity was set at 3 mm min^{-1}, which corresponds to a nominal strain rate of 1.42×10^{-3} s^{-1}, so that the deformation was dominated by rubber elasticity.

To measure the pull-off force, Stage 2 involved not only unloading but also retraction. That is, during Stage 1, the specimen was stretched beyond the unloading point, until the cratered surface was pulled off from the platform. This pull-off force is denoted as F'. To extract the suction force, we performed the same loading–unloading experiments with the vent hole open throughout the test and the collected pull-off force is denoted as F''. Representative load–displacement curves

for both cases are plotted in Fig. 2c and d where we identify the loading, unloading, and retraction stages, as well as the pull-off forces. Note that the two sets of data are qualitatively similar. Nevertheless, quantitative differences are significant enough to reveal the suction effect. For comparison purposes, the pull-off force F' was also measured when the crater was filled with air.

The experimentally collected pull-off force F' can be thought as a resultant force of the adhesion strength over the specimen/platform interface and the suction force over the crater, whereas F'' only consists of the interface adhesion. Thus, the difference in value

$$F = F' - F'' \tag{2}$$

produces the suction force inside the crater at pull-off as illustrated by the free body diagram in Fig. 2e.

In Fig. 2f, the suction force given by eqn (2) is plotted against the preload ε, which is defined as

$$\varepsilon = -\Delta L/L$$

where L is the undeformed specimen length and ΔL is the total shortening at the end of Stage 1. Results for liquid-filled craters are plotted in red, and air-filled craters are in blue. Solid dots denote results measured by the DMA while hollow dots were measured by the MTS. Note that DMA results were limited to $0 \leq \varepsilon \leq 0.32$, due to the force limitation of the DMA. At $\varepsilon \approx 0.32$, we measured the pull-off forces by both DMA and MTS. The results are in good agreement, which mutually verified each other. The plot suggests that for the same specimen, a higher suction force can be generated with higher preloads. At the same preload, the suction force is stronger in liquid-filled craters than in the air-filled ones.

2.3 Simulations

Following the framework developed in our previous study,[52] we can model the specimen to be an incompressible neo-Hookean material with shear modulus $\mu = 47.3$ kPa. Further, to simplify the analysis, we applied axisymmetry and the specimen/substrate interface was assumed to be frictionless (Fig. 3a). Also we neglected any surface tension effects simply because

$$\frac{\gamma}{a\mu} \approx \frac{2 \times 10^{-2}\ \mathrm{N\ m^{-1}}}{(10^{-2}\ \mathrm{m}) \times (4 \times 10^{4}\ \mathrm{N\ m^{-2}})} = 5 \times 10^{-5} \ll 1$$

where γ is the surface tension of PDMS.[55] We have considered the effects of surface tension only when the crater size is sufficiently small.[53] If we assume the liquid inside the crater is incompressible and there is no liquid exchange during Stage 2, it means that there should be no volume change during Stage 2. As a result, the negative pressure generated at the end of Stage 2 should be fully controlled by the crater volume at the end of Stage 1, which is determined by the preload.

We used nonlinear finite element simulations to compute the relationship between the suction force (eqn (1)) and the preload ε. All simulations were conducted using ABAQUS Version 6.14. We built an axisymmetric model with frictionless contact at the bottom and uniform compressive displacement on the top. The finite element model with a mesh formed by CAX4H elements is displayed in Fig. 3a. This mesh was selected using basic convergence tests. We used the option *FLUID CAVITY which is ideal for modeling both stages of the liquid–solid interactions.

In simulations, during unloading, liquid-filled craters recover differently from air-filled craters. The deformation snapshots of liquid- and air-filled craters are displayed in Fig. 3b. The first and last panels in each sequence are the initial (before loading) and final (end of unloading) configurations, respectively. The third panels correspond to the end of loading (Stage 1) with $\varepsilon = 0.35$, and the rest are intermediate states. A Supplementary Movie (ESI†) is provided which allows one to visualize the deformation process. At the end of the unloading (Stage 2), the finite element results indicate that the air-filled crater maintains the spherical symmetry, whereas the liquid-filled crater doesn't. Further comparisons of air-filled craters and liquid-filled craters are given in Section 2.4.

2.4 Results

In this section, we first examine the difference between air-filled craters and liquid-filled craters, and explicitly discuss the effect of the depth of water. We will then compare the experimental and simulation results for both cases. In addition, we present linear analysis results of this problem based on Eshelby's formalism.[56]

Still considering hemi-spherical craters with $\mu = 47.3$ kPa, finite element simulation results for different parameters at the end of unloading as functions of ε are plotted in Fig. 4: (a) normalized pressure drop $-\Delta p/p_a$, which is positive as Δp is

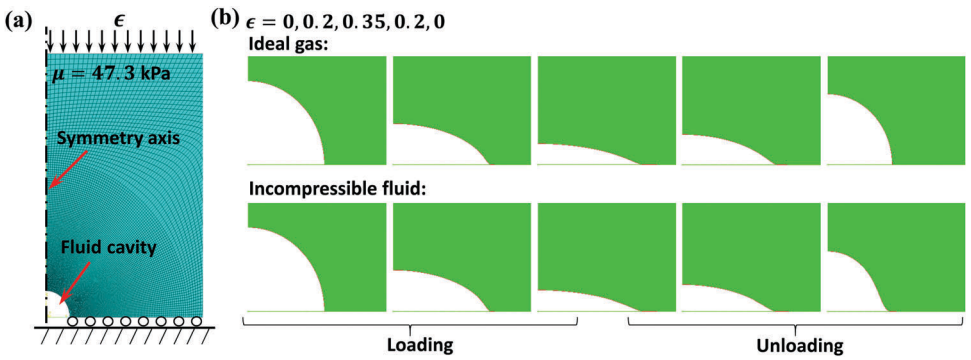

Fig. 3 (a) A finite element mesh for an axisymmetric crater model. (b) Two deformation sequences of specimens in a loading–unloading test with different fillings: the top row is for an air-filled crater and the bottom row for a liquid-filled crater.

the negative pressure, (b) phase diagram of pressure drop as a function of liquid depth h and preload ε, (c) normalized projected area A_2/A_0, and (d) normalized suction force, defined as

$$\tilde{F} = -\Delta p A_2/(p_a A_0) \quad (3)$$

Full closure of the hemi-spherical craters happens at $\varepsilon_f = 0.47$, which is independent of the type of the filling and denoted by vertical magenta dashed lines in all plots. After full closure, complete vacuum, *i.e.*, $p_2 = 0$ is achieved for craters of both fillings such that further compression will no longer increase suction. Therefore, the maximum preload was chosen as $\varepsilon = 0.5$ in all finite element simulations.

Fig. 4a clearly shows that craters of both fillings experience an increase in pressure drop with growing preload ε, whereas the liquid-filled craters exhibit a faster increase due to the stronger constraint on the polymer matrix under volume conservation, *i.e.*, $V_1 = V_2$, compared with the ideal gas relation $p_1V_1 = p_2V_2$. It can be safely predicted that both craters should achieve vacuum when fully closed, *i.e.*, $p_2 = 0$, such that the pressure drop for the air-filled crater and liquid-filled crater should be $-\Delta p = p_a$ and $-\Delta p = p_a + wh$, respectively. As shown by the blue curve in Fig. 4a, air-filled craters indeed reach $-\Delta p = p_a$ at full closure, which is consistent with our prediction. However, liquid-filled craters show a plateau of pressure drop of $-\Delta p = 2.2p_a$ at full closure, which is contradictory to the fact that the pressure drop is dependent on the liquid depth at full closure, *i.e.*, $-\Delta p = p_a + wh$. This discrepancy results from the assumption of incompressible fluid behavior which enforces zero crater volume, *i.e.*, $V_2 = 0$, throughout the unloading process in finite element simulations. Such a rigid constraint of volume conservation $V_2 = V_1 = 0$ at full closure contradicts with reality, thus the finite element results of $\varepsilon > \varepsilon_f$ in Fig. 4a (as shown by magenta makers) for liquid-filled craters are not meaningful. In reality, when the pressure inside the crater approaches the saturated vapor pressure of the liquid (denoted by p_v), the liquid vaporizes rapidly (*e.g.*, boiling), violating the assumption of incompressibility. In this case, vaporization models should be incorporated to accurately predict the negative pressure, which is out of the scope of this paper. The saturated vapor pressure of water and oil at room temperature is very small compared with atmospheric pressure, *e.g.*, $p_v \approx 2$ kPa for water and $p_v \approx 0.1$ kPa for the performance oil (99 wt% canola oil) used in our experiment according to the product sheet. Herein, we simply assume that the liquid vaporizes when the pressure inside the crater drops to zero, *i.e.*, when $p_2 = 0$ and $-\Delta p = p_a + wh$. The vaporization consideration actually sets an upper bound for the validity of the finite element results shown in Fig. 4a. For example, consider a hemisphere-cratered specimen filled with liquid at sea level, *i.e.*, $h = 0$, and the vaporization occurs when $-\Delta p = p_a$. A horizontal line of $-\Delta p = p_a$ (black dashed line) intersects with the curve of $-\Delta p/p_a(\varepsilon)$, showing a critical preload $\varepsilon_v^0 = 0.35$.

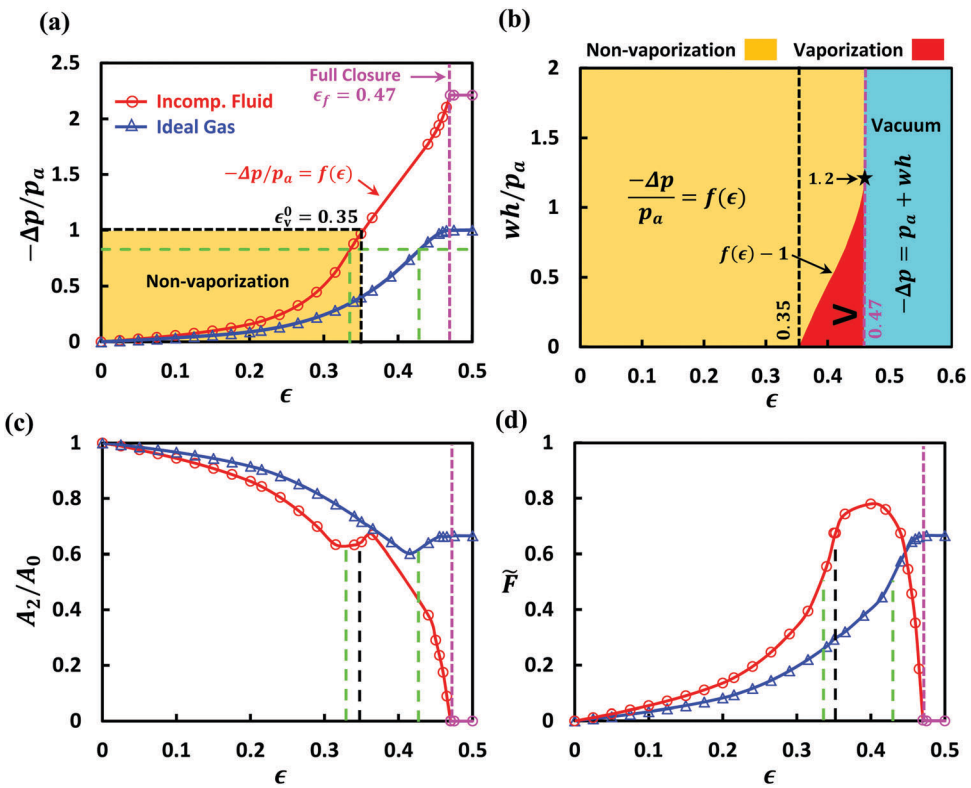

Fig. 4 End results of the loading–unloading test are computed and plotted as functions of the preload ε: (a) normalized pressure drop $-\Delta p/p_a$, (b) phase diagram of pressure drop as a function of liquid depth h and preload ε, (c) normalized projected area A_2/A_0, and (d) normalized suction force $\tilde{F} = -\Delta p A_2/(p_0 A_0)$. Craters filled with an incompressible fluid are represented by circular makers and an ideal gas by triangular markers.

When the preload is smaller than ε_v^0, we simply assume that no vaporization will happen as the pressure inside the crater is still positive, *i.e.*, $p_2 > 0$. Therefore, finite element results below ε_v^0 are valid while those above ε_v^0 are not. The critical preload for vaporization ε_v depends on the liquid depth h in that the pressure drop simply equals the ambient pressure when vaporization occurs, *i.e.*, $-\Delta p = p_a + wh$. If we simply fit the finite elements results of liquid-filled craters in Fig. 4a by using $-\Delta p/p_a = f(\varepsilon)$ for $0 \le \varepsilon \le \varepsilon_f$ (red curve), ε_v can be obtained by solving the equation $f(\varepsilon_v) = 1 + wh/p_a$ for a given liquid depth h. When $\varepsilon < \varepsilon_v$, *i.e.* when $f(\varepsilon) < f(\varepsilon_v) = 1 + wh/p_a$, no vaporization would occur. As a result, we can write the pressure drop as a function of liquid depth h and preload ε:

$$-\frac{\Delta p}{p_a}(\varepsilon, h) = \begin{cases} f(\varepsilon) & 0 \le \varepsilon < \varepsilon_v^0, \forall h \\ f(\varepsilon) & \varepsilon_v^0 \le \varepsilon < \varepsilon_f \ \&\ wh/p_a > f(\varepsilon) - 1 \\ \text{Vaporization, no solution} & \varepsilon_v^0 \le \varepsilon < \varepsilon_f \ \&\ wh/p_a \le f(\varepsilon) - 1 \\ 1 + wh/p_a & \varepsilon \ge \varepsilon_f \end{cases} \quad (4)$$

Eqn (4) can be illustrated by a phase diagram as Fig. 4b where the horizontal axis is the preload ε and the vertical axis is the normalized liquid depth wh/p_a. The solution to pressure drop will be different in different regimes. The brown regimes are non-vaporization zones where the pressure drop is simply characterized by $-\Delta p/p_a = f(\varepsilon)$, the red regime is where vaporization would occur, and the cyan regime represents complete vacuum. When $\varepsilon < \varepsilon_v^0 = 0.35$, the pressure inside the crater after unloading is always above zero, *i.e.*, non-vaporization, and the pressure drop is given by $-\Delta p/p_a = f(\varepsilon)$ which is independent of the liquid depth h as the hydrostatic pressure wh does not deform the incompressible specimen. When $\varepsilon_v^0 \le \varepsilon < \varepsilon_f = 0.47$, vaporization occurs when $-\Delta p \ge p_a + wh$, *i.e.*, $wh/p_a \le -\Delta p/p_a - 1 = f(\varepsilon) - 1$, as highlighted by the red regime. Hence, when $wh/p_a > f(\varepsilon) - 1$, no vaporization happens and our finite element results are useful. Interestingly, according to the finite element results in Fig. 4a, when the preload approaches ε_f, the pressure drop is capped at $-\Delta p/p_a = 2.2$, corresponding to a maximum normalized liquid depth for vaporization $wh/p_a = 1.2$. It means that for normalized liquid depth higher than 1.2, the craters will be fully closed prior to the significant vaporization of the liquid. Such a critical liquid depth is about 12 m for water if we simply take $w \approx 10^4$ N m^{-3}. When $\varepsilon \ge \varepsilon_f$, the hemispherical crater attains full closure and realizes complete vacuum, giving rise to $-\Delta p = p_a + wh$, regardless of the flawed finite element simulation at full closure. Therefore, when the crater is fully closed, craters in deeper waters will produce a higher suction force. We need to point out again that the vaporization discussed in this paper refers to the rapid liquid-to-vapor phase transition, *e.g.*, boiling, rather than the slow evaporation that is always ongoing on the liquid surface.

After fully understanding the pressure drop, we are ready to look at the suction force $\tilde{F}$ given in eqn (3). The projected area A_2 is affected by the instabilities in the craters subjected to a large preload. In Fig. 4a, the horizontal dashed green line represents the critical Δp_c, beyond which the hemispherical shape of the crater breaks down upon unloading, irrespective of the filling or the depth of the liquid. This critical load $-\Delta p_c = 0.83 p_a$ is obtained by analyzing the surface instability of a spherical void in an infinitely large block (Appendix A).[57,58] And the corresponding critical preload ε_c is 0.33 and 0.43 for liquid- and air-filled craters, respectively.

As observed in finite element simulation results in Fig. 3b, once instability happens upon unloading, the partially recovered crater shows a shallower but wider profile, giving rise to increased projected area, *i.e.* larger A_2. This explains the slight increase of the A_2/A_0 at ε_c for both liquid-filled and air-filled craters plotted in Fig. 4c. However, for liquid-filled craters, the instability induced increase in A_2 doesn't last. This is because the volume conservation constraint also gets stronger with increasing preload ε and eventually overwhelms other factors, leading to the re-decrease of A_2, as shown in Fig. 4c. For liquid-filled craters, A_2 eventually drops to 0 with fully closed craters due to the volume conservation enforced in the finite element simulation. The increasing Δp and the overall decreasing A_2 together produce an $\tilde{F}$ that varies non-monotonically with ε for liquid-filled craters, as plotted in Fig. 4d. But as we discussed before, for liquid-filled craters at sea level, vaporization begins at $\varepsilon_v^0 = 0.35$, which is represented by the black dashed lines in Fig. 4c and d. Therefore, the finite element results for A_2 and $\tilde{F}$ of liquid filled craters (the red curves) are no longer meaningful beyond the black dashed lines. However, the blue curves for air-filled craters should be valid all the way till full closure, *i.e.* $\varepsilon_f = 0.47$.

A comparison of simulation (solid curves) and experimental (circular markers) results for hemi-spherical craters is conducted in Fig. 5a, where the suction force is plotted *versus* the preload ε. Results corresponding to liquid-filled craters are plotted in red, and air-filled craters are in blue for comparison. In the range of $0 \le \varepsilon \le 0.3$, experimental and simulation results are in good agreement for both types of crater. This validates the theoretical framework we developed and also justifies applying the framework on craters of other shapes under moderate preload. We also calculated the suction force using linear (infinitesimal strain) analysis based on Eshelby's formalism.[56] This approach is possible because of the assumptions that the specimen is large compared with the crater, the interface is frictionless, and the surface tension effects are negligible. Details of this analysis are presented in Appendix B, and the results (dotted curves) are shown in Fig. 5a. It is clear that the linear analysis is valid for small strains, and deviates significantly from the experimental and simulation results for $\varepsilon > 0.1$, and therefore its usefulness is rather limited.

Under large preload, especially when the crater reaches full closure, the finite element simulation shows considerable discrepancy from experimental results for both air-filled craters and liquid-filled craters. For air-filled craters, we recognize that

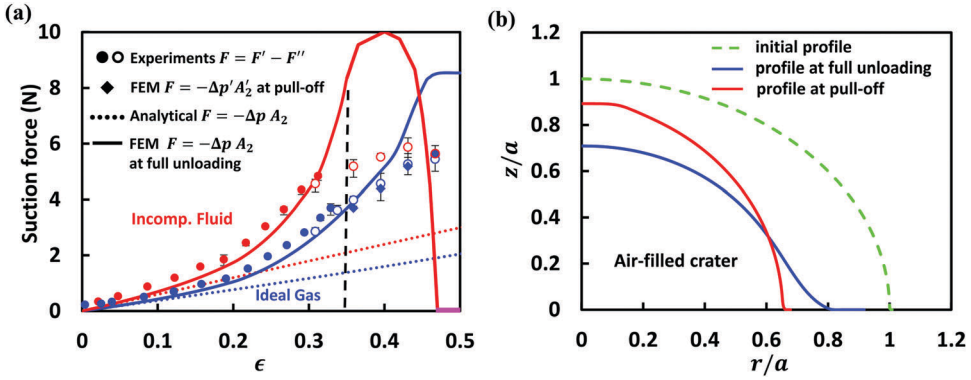

Fig. 5 (a) Comparisons of suction forces obtained by experimental measurements (circular markers), analytical modeling (dashed curves) and finite element simulation (solid curves and diamond markers). Craters filled with an incompressible fluid are represented by red ($0 \le \varepsilon < \varepsilon_f$) and magenta ($\varepsilon_f \le \varepsilon < 0.5$) and an ideal gas by blue. (b) Profiles of air-filled craters under undeformed (black dashed curve), full unloading (blue curve), and pull-off (red curve) conditions.

the source of the discrepancy comes from the different definitions of suction force used in experiments and simulations. In experiments, $F' - F''$ (eqn (2)) represents the suction force inside the crater at pull-off, while in simulations, $-\Delta p A_2$ (eqn (1)) is used to calculate suction force at the end of unloading, without any retraction. At small to moderate preloads, it is fair to argue that the crater has a similar configuration at pull-off and full unloading, so that

$$F' - F'' \approx -\Delta p A_2 \tag{5}$$

is expected. This is true in the loading range $0 \le \varepsilon \le 0.3$ based on the observation from Fig. 5a. However, this approximation will no longer hold when the crater shapes are very different at pull-off and full unloading. To verify this hypothesis, we applied experimentally measured retraction strain at pull-off, ε_t, in simulation beyond full unloading. The resulting suction forces, $F = -\Delta p' A_2'$, are plotted as solid blue diamonds in Fig. 5a, where $\Delta p'$ and A_2' represent the finite element results of pressure drop inside the crater and the projected area of the crater at pull-off, respectively, at the pull-off point. Fig. 5b depicts the profiles of air-filled craters at unloading (blue curve) and pull-off (red curve) and a visible difference can be found at full closure. In Fig. 5a, the good agreement between $F = -\Delta p' A_2'$ (the diamond markers) and $F' - F''$ (the circular markers) indicates that, for air-filled craters, the discrepancy between the finite element results of suction force (the solid curve) and the experimentally measured pull-off force (the circular markers) can be fully explained by the difference in unloading *vs.* pull-off points. In other words, for air-filled craters, our finite element simulation is valid all the way up to the preload that fully closes the crater in terms of predicting the suction force at full unloading before retraction.

For liquid-filled craters, finite element results start to deviate from experiments when the preload $\varepsilon > 0.3$. In addition to the difference between suction and pull-off forces discussed above, there are other reasons which are only pertinent to liquid fillings. As we already know, the liquid inside the crater may undergo liquid-to-vapor phase transition when the preload approaches the critical value $\varepsilon_v^0 = 0.35$ as experiments are carried at sea level in air, *i.e.*, $h = 0$. Vaporization would increase the pressure inside the crater, thus compromising the suction force and hence the measured pull-off force. Moreover, the critical preload for vaporization $\varepsilon_v^0 = 0.35$ was obtained without considering the retraction strain ε_t in the simulation while the experimental results were measured at the pull-off points. Applying retraction strain to the specimen beyond full unloading will further reduce the liquid pressure inside the crater, causing the liquid to vaporize prior to the critical preload $\varepsilon_v^0 = 0.35$. This can explain why deviation between finite element results and experiments starts after $\varepsilon = 0.3$ rather than 0.35. Further discussions regarding the effects of retraction on vaporization are offered in Section 3. Thus, for liquid-filled craters, the applicability of the finite element simulation under large preloads is limited to moderate preloads. For the specimens used in this paper, the deviation between finite element simulations and experiments occurs at $\varepsilon \approx 0.3$. One should note that the deviation may occur at different preloads ε if the specimens are made of different materials or the crater shape is different or the specimen is at different depths of liquid.

It is also obvious that experimentally, craters with both fillings produced similar suction forces after full closure, validating our expectation that at full closure, the pressure drop in both types of crater should equal the ambient pressure at sea level, *i.e.*, $-\Delta p = p_a$.

To accurately predict the pull-off force, one needs the traction-separation behavior of the specimen/platform interface, and the vaporization process of the liquid, which are out of our current focus. So, for Section 3, we would focus on the study of the suction force given by eqn (1).

3. Spherical-cap-shaped (SCS) craters

In this section, we extend the experimental and simulation approach established for hemi-spherical craters to spherical-cap-shaped (SCS) craters that are filled with an incompressible fluid. Our objective is to investigate the effects of crater shape and preload so we fix the material modulus to be $\mu = 47.3$ kPa.

In fact, according to dimensional analysis, the pressure drop and hence the suction force for underwater craters have to scale with the modulus of the specimen μ as p_a is not relevant except when considering vaporization or full closure. In this section, however, we will continue to use p_a in the normalization just to be consistent with Fig. 4, where air-filled craters were compared with liquid-filled ones. Since our analysis is limited to large specimens, the only dimensionless geometric parameter involved is the crater aspect ratio, *i.e.* b/a, where a is the crater base radius and b is the crater height (Fig. 6a). Finite element results of pressure drops as a function of preload for SCS craters with various aspect ratios (b/a = 0.1, 0.2, 0.3, 0.4, 0.5, 0.6, 0.7, 0.8, 0.9 and 1) are plotted in Fig. 6b. For each b/a, the location of the preload of full closure is marked by the arrow. It is evident that shallower craters reach full closure at smaller preloads than the deeper ones. Particularly, SCS craters with aspect ratio $b/a < 0.5$ reach full closure before $\varepsilon_v^0 = 0.35$, meaning that no vaporization will take place before such craters are fully closed. For SCS craters with aspect ratios $b/a \geq 0.5$, our simulation result indicates that they have the same critical preload for vaporization, *i.e.* the curves all intersect at $\varepsilon_v^0 = 0.35$ as evidenced in Fig. 6b. At this moment, we do not have an explanation for this observation. To validate our finite element simulation results for SCS craters with different aspect ratios, we conducted extra experiments on two SCS craters with aspect ratios b/a = 0.25 and 0.5. To eliminate the effect of A_0, the crater base radius a = 6.35 mm was fixed in all three specimens. All experiments were conducted in air with liquid filling at sea level at room temperature. Numerical (curves and diamond markers) and experimental (circular markers) results of suction forces for SCS craters with b/a = 0.25, 0.5, and 1 are plotted together in Fig. 6c. It is obvious that the simulated suction forces only agree with measured pull-off forces at small to moderate preloads. The shallower the crater, the earlier the deviation. For craters with b/a = 0.25, 0.5 and 1, the preload at deviation are ε_d = 0.05, 0.13 and 0.3, respectively. For the hemispherical crater, *i.e.*, b/a = 1, towards the end of Section 2.4, this discrepancy was partially attributed to the possible vaporization when the preload approaches $\varepsilon_v^0 = 0.35$ (as shown by the black dashed line in Fig. 6c). However, for craters with b/a = 0.25 and 0.5, no vaporization would occur under such small preload, *i.e.*, ε_d = 0.05 and 0.13, according to Fig. 6b. Therefore, we hypothesize that the deviation is due to the difference between simulated suction forces given by eqn (1) and measured pull-off forces extracted using eqn (2). To prove it, we added a retraction stage in finite element simulations where the applied retraction strain is the same as the pull-off strain in experiments. In this way, we can numerically obtain the suction force at the pull-off point for craters with b/a = 0.25 and 0.5. Simulated results are plotted as diamond markers in Fig. 6c, which agree well with the experiments. This agreement validates our hypothesis and implies that our finite

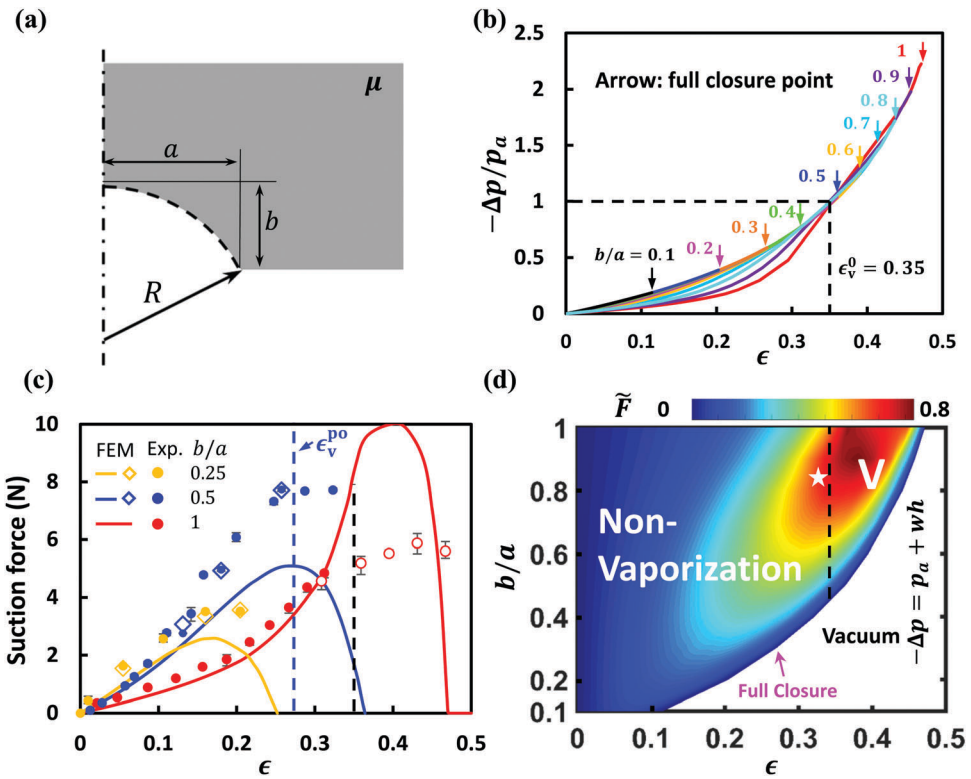

Fig. 6 (a) Schematics of a spherical-cap-shaped (SCS) crater. (b) Finite element results of pressure drop as a function of preload for various SCS craters. Arrows indicate the full closure point. (c) Suction force as a function of applied strain for SCS craters with aspect ratios of b/a = 0.25, 0.5 and 1. Curves and diamonds represent finite element results at full unloading and pull-off point, respectively. Solid (DMA) and open (MTS) circular dots are experimental data. (d) A contour plot for the normalized suction force at full unloading $\tilde{F} = -\Delta p A_2/(p_a A_0)$ as a function of b/a and ε. The white star highlights the highest suction force in the non-vaporization regime while the capital "V" represents the vaporization zone when $\varepsilon > \varepsilon_v^0 = 0.35$.

element simulated suction forces (the solid curves), which are defined to be the attachment force at the end of unloading and before retraction, are valid. But adding retraction strain for fluid-filled craters should be conducted with caution because the retraction strain would further reduce the hydrostatic pressure in the liquid, expediting vaporization. For instance, for craters with $b/a = 0.5$ under preload $\varepsilon = 0.29$, no vaporization happens at the end of unloading. However, after applying retraction, the pressure drop further increases beyond 1, which means although vaporization does not take place at the end of unloading, it could happen at the pull-off point. Therefore, the critical preload for vaporization at pull-off, ε_v^{po}, is smaller than that at the end of unloading, ε_v. We use a blue dashed line to represent ε_v^{po} in Fig. 6c. To the left of this line, finite element simulated suction forces at the pull-off point (blue diamonds) and experimentally measured pull-off forces (blue dots) match perfectly. To the right of this line, evaporation kicks in so the finite element simulation becomes useless. For craters with $b/a = 0.25$, the maximum preload used in the experiment was 0.2, by which no vaporization would occur according to the finite element results at the pull-off point. Therefore, the modified finite element results (yellow diamonds) can fully capture the measured pull-off forces (yellow dots). From such an exercise, we learned that as long as the crater is not fully closed and the liquid inside remains as incompressible, *i.e.* no vaporization, the discrepancy between the finite element curves and experimental dots in Fig. 6c purely stems from the different definitions of suction force, rather than the numerical approach itself. Therefore, it is reasonable to believe that the finite element curves before the black dashed curve ($\varepsilon_v^0 = 0.35$) are able to capture the true suction forces at the end of unloading.

To summarize the effects of preload and aspect ratio on suction forces, we offer a contour plot for the normalized suction force $\tilde{F}$ at full unloading (eqn (3)) in Fig. 6d. First, the white regime represents vacuum due to full closure. If the crater reaches vacuum, the pressure drop is simply given by $-\Delta p = p_a + wh$, which is obviously dependent on the depth of the liquid, h. When $h = 0$ and the crater reaches vacuum, our previous results for air-filled craters at full closure (Fig. 6b in ref. 52) are applicable. Second, before the crater is fully closed, the liquid vaporizes when the preload is beyond $\varepsilon_v^0 = 0.35$ when $h = 0$ (shown by the black dashed curve). Note that ε_v changes with h and the dependence is shown in Fig. 4b. Our simulation results beyond ε_v are not meaningful due to liquid vaporization. Third, below ε_v is the non-vaporization zone, where our numerical results have been validated by experiments as discussed in Fig. 6c and such results are independent of h as discussed in Section 2.4. It is clear that the suction force has a non-monotonic dependence on the aspect ratio of the craters. The highest suction force $\tilde{F} = 0.69$ can be generated by a SCS crater with $b/a = 0.8$ under preload $\varepsilon \approx 0.34$, as highlighted by the white star in Fig. 6d.

4. Conclusion

In this paper, we try to elucidate adhesion generated by a cratered surface under water or more generally, immersed in an incompressible fluid. Such enhanced adhesion is purely enabled by suction forces due to pressure difference between the crater and the ambient, thus is reversible. We restricted ourselves to isolated macroscopic SCS craters, for which surface tension and other microscopic mechanisms were assumed to be negligible. The restriction to SCS craters is dictated by manufacturing considerations, but of course one can consider other shapes. Both experimental and simulation results focused on specimens resting on frictionless substrates with small vent holes. Clearly, friction would weaken the suction effect as it requires a large force to close the crater. Therefore, reducing friction should be desirable for all practical purposes. Vent holes are necessary to satisfy our assumption of zero resistance to fluid flow. In reality, nonzero resistance may exist and hence would further weaken the suction effects. Under such idealized assumptions, our key findings are summarized as follows:

- As long as the specimen is immersed in the incompressible fluid and the fluid inside the crater does not vaporize or fully disappear, the suction forces generated are independent of the depth of the liquid and can be confidently predicted by the framework established in this paper even under a large preload.
- In this case, suction force measurement for underwater craters can be simply carried out in air with the liquid filled in the crater.
- In this case, the suction force produced by underwater craters scales with the modulus of the polymer material.
- In this case, for specimen of $\mu = 47.3$ kPa examined in this paper, with the same crater geometry, underwater craters are capable of producing stronger suction force than craters in air.
- In this case, for specimen of $\mu = 47.3$ kPa examined in this paper with liquid filling, the largest suction forces $\tilde{F} = 0.69$ can be generated by a SCS crater with $b/a = 0.8$ under preload $\varepsilon \approx 0.34$.
- If the crater is fully closed during loading, vacuum is generated in the crater and the resulting suction force should be independent of the filler but dependent on the depth of the liquid.
- The depth of the liquid and the preload together dictate when the liquid inside the crater would vaporize. When $wh/p_a > 1.2$, the liquid would never vaporize at the end of unloading even up to full closure.

Conflicts of interest

There are no conflicts to declare.

Appendix A

On the surface of the spherical void in an infinitely large block, traction $-\Delta p$ is exerted in the normal direction, and one has principal stretches λ_r, λ_θ and λ_ϕ on the surface. Before the spherical symmetry breaks down, for incompressible Neo-Hookean block with shear modulus μ, Δp can be written as

$$-\frac{\Delta p}{\mu} = \frac{4\lambda_\theta^3 + 1}{2\lambda_\theta^4} - \frac{5}{2} \quad \text{(A1)}$$

The critical condition for a surface crease setting in is given as[58]

$$\frac{\lambda_r}{\lambda_\theta} = 2.4 \tag{A2}$$

Considering the spherical symmetry as well as incompressibility of the block material, before the crease sets in, the principal stretches follow

$$\lambda_\theta = \lambda_\phi = \frac{1}{\sqrt{\lambda_r}} \tag{A3}$$

Combining eqn (A1)–(A3) leads to the critical load $\Delta p_c = -1.78\mu$, and $-\Delta p_c/p_a = 0.83$ when $\mu = 47.3$ kPa.

Appendix B

In this appendix, we derive an analytical solution of classical linear elasticity theory for the pressure drop of an underwater isolated hemi-spherical crater in a semi-infinite specimen under remote compressive load. We take advantage of the assumption that the contact between the specimen and the substrate is frictionless. This allows us to replace the problem of a semi-infinite specimen containing a hemi-spherical crater with an infinite specimen containing a spherical cavity. This problem is straightforward to analyze using Eshelby's formalism.[56]

According to eqn (2), we need to calculate V_1 and V_2. To compute ΔV_1, we subject the infinite specimen to remote uniaxial compressive strain ε. For this case, the specimen has Poissons's ratio equal to 0.5 such that Eshelby's formalism yields

$$\Delta V_1 = -\frac{3}{4}\varepsilon V_0. \tag{B1}$$

To compute ΔV_2, we subject the cavity to the surface traction

$$\boldsymbol{t} = (p_a - p_2)\boldsymbol{n} = -\Delta p\boldsymbol{n}$$

where $\boldsymbol{n}$ is the outward normal. As far as ΔV_2 is concerned, this problem is equivalent to the superposition of two problems. In the first problem, the specimen is uniformly loaded by $-\Delta p$ on both cavity and remote surfaces. In the second problem, the cavity surface is traction-free and the remote surface is subjected to Δp. As a result, we obtain

$$\Delta V_2 = \frac{3}{4}\frac{\Delta p}{\mu}V_0. \tag{B2}$$

Since the fluid in the cavity is incompressible and there is no fluid exchange during unloading, we have

$$\Delta V_1 = \Delta V_2. \tag{B3}$$

Combining eqn (A1)–(A3), one obtains the pressure drop in the crater upon unloading as

$$\Delta p = -\varepsilon\mu. \tag{B4}$$

Note that in our previous work,[52] when the crater is filled with an ideal gas, the pressure drop in the crater upon unloading is

$$\Delta p = -\frac{1}{2}\left[\left(1+\frac{4\mu}{3p_a}\right) - \sqrt{\left(1+\frac{4\mu}{3p_a}\right)^2 - 8(1-\nu)\frac{\mu}{p_a}\varepsilon}\right]p_a. \tag{B5}$$

Acknowledgements

The authors acknowledge the support from the National Science Foundation (NSF) Division of Civil, Mechanical and Manufacturing Innovation (CMMI) award (Grant No. 1663551). Shutao Qiao and Liu Wang acknowledge the Warren A. and Alice L. Meyer endowed graduate fellowship awarded by the Cockrell School of Engineering at the University of Texas at Austin. Kyoung-Ho Ha acknowledges the Philip C. and Linda L. Lewis Foundation Graduate Fellowship in Mechanical Engineering at the University of Texas at Austin.

References

1 C. Menon, M. Murphy and M. Sitti, Gecko inspired surface climbing robots, IEEE International Conference on Robotics and Biomimetics, IEEE, 2004, pp. 431–436.
2 H. Kim, D. Kim, H. Yang, K. Lee, K. Seo, D. Chang and J. Kim, *J. Mech. Sci. Technol.*, 2008, **22**, 1490–1498.
3 S. Seo, J. Lee, K.-S. Kim, K. H. Ko, J. H. Lee and J. Lee, *ACS Appl. Mater. Interfaces*, 2014, **6**, 1345–1350.
4 W.-Y. Chang, Y. Wu and Y.-C. Chung, *Nano Lett.*, 2014, **14**, 1546–1550.
5 H. Lee, D. S. Um, Y. Lee, S. Lim, H. J. Kim and H. Ko, *Adv. Mater.*, 2016, **28**, 7457–7465.
6 Y.-C. Chen and H. Yang, *ACS Nano*, 2017, **11**, 5332–5338.
7 M. K. Choi, O. K. Park, C. Choi, S. Qiao, R. Ghaffari, J. Kim, D. J. Lee, M. Kim, W. Hyun, S. J. Kim, H. J. Hwang, S.-H. Kwon, T. Hyeon, N. Lu and D.-H. Kim, *Adv. Healthcare Mater.*, 2016, **5**, 80–87.
8 M. K. Kwak, H. E. Jeong and K. Y. Suh, *Adv. Mater.*, 2011, **23**, 3949–3953.
9 M. Cui, S. Ren, S. Wei, C. Sun and C. Zhong, *APL Mater.*, 2017, **5**, 116102.
10 J. Li, A. Celiz, J. Yang, Q. Yang, I. Wamala, W. Whyte, B. Seo, N. Vasilyev, J. Vlassak and Z. Suo, *Science*, 2017, **357**, 378–381.
11 Y. Zhao, Y. Wu, L. Wang, M. Zhang, X. Chen, M. Liu, J. Fan, J. Liu, F. Zhou and Z. Wang, *Nat. Commun.*, 2017, **8**, 2218.
12 K. Autumn, Y. A. Liang, S. T. Hsieh, W. Zesch, W. P. Chan, T. W. Kenny, R. Fearing and R. J. Full, *Nature*, 2000, **405**, 681–685.
13 D. J. Irschick, C. C. Austin, K. Petren, R. N. Fisher, J. B. Losos and O. Ellers, *Biol. J. Linn. Soc.*, 1996, **59**, 21–35.
14 K. Autumn, M. Sitti, Y. A. Liang, A. M. Peattie, W. R. Hansen, S. Sponberg, T. W. Kenny, R. Fearing, J. N. Israelachvili and R. J. Full, *Proc. Natl. Acad. Sci. U. S. A.*, 2002, **99**, 12252–12256.

15 E. Arzt, S. Gorb and R. Spolenak, *Proc. Natl. Acad. Sci. U. S. A.*, 2003, **100**, 10603–10606.
16 R. Spolenak, S. Gorb, H. Gao and E. Arzt, *Proc. R. Soc. A*, 2005, **461**, 305–319.
17 M. P. Murphy, S. Kim and M. Sitti, *ACS Appl. Mater. Interfaces*, 2009, **1**, 849–855.
18 K. Jin, Y. Tian, J. S. Erickson, J. Puthoff, K. Autumn and N. S. Pesika, *Langmuir*, 2012, **28**, 5737–5742.
19 H. Lee, B. P. Lee and P. B. Messersmith, *Nature*, 2007, **448**, 338–341.
20 M. D. Bartlett, A. B. Croll, D. R. King, B. M. Paret, D. J. Irschick and A. J. Crosby, *Adv. Mater.*, 2012, **24**, 1078–1083.
21 M. P. Murphy, B. Aksak and M. Sitti, *Small*, 2009, **5**, 170–175.
22 Y. Mengüç, S. Y. Yang, S. Kim, J. A. Rogers and M. Sitti, *Adv. Funct. Mater.*, 2012, **22**, 1246–1254.
23 S. Chary, J. Tamelier and K. Turner, *Smart Mater. Struct.*, 2013, **22**, 025013.
24 S. Buhl, C. Greiner, A. D. Campo and E. Arzt, *Int. J. Mater. Res.*, 2009, **100**, 1119–1126.
25 N. Cadirov, J. A. Booth, K. L. Turner and J. N. Israelachvili, *ACS Appl. Mater. Interfaces*, 2017, **9**, 14497–14505.
26 N. S. Pesika, H. Zeng, K. Kristiansen, B. Zhao, Y. Tian, K. Autumn and J. Israelachvili, *J. Phys.: Condens. Matter*, 2009, **21**, 464132.
27 W. M. Kier and A. M. Smith, *Biol. Bull.*, 1990, **178**, 126–136.
28 W. M. Kier and A. M. Smith, *Integr. Comp. Biol.*, 2002, **42**, 1146–1153.
29 F. Tramacere, L. Beccai, M. Kuba, A. Gozzi, A. Bifone and B. Mazzolai, *PLoS One*, 2013, **8**, e65074.
30 D. K. Wainwright, T. Kleinteich, A. Kleinteich, S. N. Gorb and A. P. Summers, *Biol. Lett.*, 2013, **9**, 20130234.
31 A. M. Smith, *J. Exp. Biol.*, 1991, **157**, 257–271.
32 A. Smith, *J. Exp. Biol.*, 1996, **199**, 949–958.
33 L. Afferrante, G. Carbone, G. Demelio and N. Pugno, *Tribol. Lett.*, 2013, **52**, 439–447.
34 D. Ge, T. Matsuno, Y. Sun, C. Ren, Y. Tang and S. Ma, *Vacuum*, 2015, **116**, 13–20.
35 J. Liu, K. Tanaka, L. Bao and I. Yamaura, *Vacuum*, 2006, **80**, 593–598.
36 A. Del Campo, C. Greiner and E. Arzt, *Langmuir*, 2007, **23**, 10235–10243.
37 A. del Campo, C. Greiner, I. Álvarez and E. Arzt, *Adv. Mater.*, 2007, **19**, 1973–1977.
38 S. C. Fischer, K. Groß, O. Torrents Abad, M. M. Becker, E. Park, R. Hensel and E. Arzt, *Adv. Mater. Interfaces*, 2017, **4**, 1700292.
39 S. Baik, J. Kim, H. J. Lee, T. H. Lee and C. Pang, *Adv. Sci.*, 2018, 1800100.
40 L. Heepe, M. Varenberg, Y. Itovich and S. N. Gorb, *J. R. Soc., Interface*, 2011, **8**, 585–589.
41 H. Gao and H. Yao, *Proc. Natl. Acad. Sci. U. S. A.*, 2004, **101**, 7851–7856.
42 A. Del Campo and E. Arzt, *Macromol. Biosci.*, 2007, **7**, 118–127.
43 E. P. Chan, C. Greiner, E. Arzt and A. J. Crosby, *MRS Bull.*, 2007, **32**, 496–503.
44 C. Greiner, A. D. Campo and E. Arzt, *Langmuir*, 2007, **23**, 3495–3502.
45 T. Kim, J. Park, J. Sohn, D. Cho and S. Jeon, *ACS Nano*, 2016, **10**, 4770–4778.
46 H. E. Jeong and K. Y. Suh, *Nano Today*, 2009, **4**, 335–346.
47 S. Baik, D. W. Kim, Y. Park, T.-J. Lee, S. Ho Bhang and C. Pang, *Nature*, 2017, **546**, 396–400.
48 S. Akerboom, J. Appel, D. Labonte, W. Federle, J. Sprakel and M. Kamperman, *J. R. Soc., Interface*, 2015, **12**, 20141061.
49 G. Nanni, D. Fragouli, L. Ceseracciu and A. Athanassiou, *Appl. Surf. Sci.*, 2015, **326**, 145–150.
50 F. Tramacere, N. M. Pugno, M. J. Kuba and B. Mazzolai, *Interface Focus*, 2015, **5**, 20140050.
51 A. Majumder, A. Sharma and A. Ghatak, *Langmuir*, 2009, **26**, 521–525.
52 S. Qiao, L. Wang, H. Jeong, G. J. Rodin and N. Lu, *J. R. Soc., Interface*, 2017, **14**, 20170377.
53 L. Wang, S. Qiao and N. Lu, *Extreme Mech. Lett.*, 2017, **15**, 130–138.
54 J. Zimmermann and M. Stommel, *Arch. Appl. Mech.*, 2013, **83**, 293–302.
55 J. Brandrup, E. H. Immergut, E. A. Grulke, A. Abe and D. R. Bloch, *Polymer handbook*, Wiley, New York *etc.*, 1989.
56 J. D. Eshelby, *Proc. R. Soc. London, Ser. A*, 1957, **241**, 376–396.
57 S. Cai, K. Bertoldi, H. Wang and Z. Suo, *Soft Matter*, 2010, **6**, 5770–5777.
58 W. Hong, X. Zhao and Z. Suo, *Appl. Phys. Lett.*, 2009, **95**, 111901.

Electronic Supplementary Material (ESI) for Soft Matter.

Supplementary Information of "Suction Effects of Craters Underwater"

Shutao Qiao[a], Liu Wang[a], Kyoungho Ha[b], Nanshu Lu*[a, b, c, d]

[a]*Center for Mechanics of Solids, Structures and Materials, Department of Aerospace Engineering and Engineering Mechanics, the University of Texas at Austin, Austin TX 78712, US.*

[b]*Department of Mechanical Engineering, the University of Texas at Austin, Austin TX 78712, US.*

[c]*Department of Biomedical Engineering, the University of Texas at Austin, Austin TX 78712, US.*

[d]*Texas Materials Institute, the University of Texas at Austin, Austin TX 78712, US.*

* Corresponding author: nanshulu@utexas.edu, 512-471-4208, 210 E. 24th St, Austin, TX 78712

S1. Raw finite element simulation results

This section contains tables of raw finite element simulation results that are referred in the main text. Table S1 shows the nominal suction force $\hat{F}$ of unreinforced spherical-cap-shaped (SCS) craters as a function of the crater aspect ratio α and the dimensionless stiffness parameter β. All specimens in Table S1 were preloaded with the nominal strain $\Theta = \Theta_m$. Based on the data in Table S1, a contour plot of $\hat{F}$ was made and presented in Fig. 6b in the main text. Table S2 corresponds to Fig. 8b in the main text. It lists all the simulation results of the nominal suction force $\hat{F}$ of a reinforced hemi-spherical crater with shear modulus $\mu = p_0$ (i.e. $\alpha = \beta = 1$) as a function of the reinforcement parameters α' and β'. The background color has the same meaning used in Fig. 8b: the green color represents craters that exhibit instabilities upon both loading and unloading, the red color indicates craters that exhibit instabilities upon unloading only, and the blue color corresponds to stable craters. "NA" denotes a finite element job that diverges before full unloading. In Table S3, the nominal suction force $\hat{F}$ of unreinforced hemi-spheroidal craters with different α and β were collected. Data in Table S3 produces the contour plot Fig. S1b, which will be discussed later.

Table S1. Finite element simulation results of unreinforced SCS craters at $\Theta = \Theta_m$

$\hat{F}$		β							
		0.2	0.5	1	2	4	6	8	10
α	0.049783	0	0	0	0	0.310271	0.609197	0.609197	1
	0.09999	0	0	0	0	0.610301	0.829661	0.901584	1
	0.176327	0	0	0	0.527908	0.872468	0.942231	0.963738	0.994089
	0.249328	0	0	0.110721	0.760677	0.933554	0.96735	0.978581	0.9938
	0.267949	0	0	0.229163	0.791353	0.948403	0.977824	0.98262	0.993228
	0.315299	0	0	0.457389	0.860282	0.959966	0.978792	0.983527	0.99774
	0.36397	0	0	0.587125	0.900493	0.975772	0.984062	0.99217	0.993411
	0.414214	0	0	0.688574	0.91581	0.965588	0.985403	0.991935	0.991935
	0.466308	0	0.079166	0.757595	0.925787	0.966642	0.974824	0.980546	0.99061
	0.520567	0	0.256136	0.808409	0.934979	0.96422	0.975524	0.980349	0.99041
	0.57735	0	0.401606	0.827734	0.914991	0.956574	0.9675	0.980214	0.990826
	0.63707	0	0.571608	0.851765	0.9085	0.9653	0.9632	0.9789	0.981755
	0.700208	0	0.60989	0.857284	0.902963	0.945565	0.957316	0.978494	0.9787
	0.767327	0	0.683776	0.845801	0.8913	0.9386	0.9501	0.9646	0.975716
	0.8391	0	0.724998	0.80161	0.861889	0.932589	0.949021	0.959904	0.963877
	0.900404	0	0.726778	0.762221	0.839201	0.910794	0.9391	0.955602	0.9587
	1	0	0.65419	0.690264	0.818424	0.903924	0.939446	0.956766	0.967559

Table S2. Finite element simulation results of reinforced hemi-spherical craters at $\Theta = \Theta_m$

$\hat{F}$		β'										
		1	2	3	4	5	6	8	10	20	40	80
α'	0.01	0.692958	0.701492	NA	NA	NA	NA	NA	NA	NA	NA	NA
	0.015	0.692958	0.702884	0.764178	NA	NA	NA	NA	NA	0.917544	NA	1.072737
	0.02	0.692958	0.705822	0.779385	NA	NA	NA	NA	NA	NA	1.09307	NA
	0.025	0.692958	0.721489	0.786343	NA	NA	NA	NA	NA	1.024023	1.092736	NA
	0.03	0.692958	0.712848	0.736633	0.849924	0.883666	0.906161	NA	NA	NA	NA	NA
	0.035	0.692958	0.718483	0.74342	0.855849	0.899487	NA	0.961659	0.992165	1.047798	1.034452	NA
	0.04	0.692958	0.729041	0.759017	0.848359	0.904894	0.93715	0.976462	1.005026	1.052553	1.052553	NA
	0.045	0.692958	0.722019	0.747672	0.768905	0.792344	0.928099	0.972324	1.027	0.976927	0.976927	NA
	0.05	0.692958	0.732289	NA	0.787044	0.816408	0.866547	0.939709	0.965676	0.987199	0.938918	0.966761
	0.055	0.692958	0.725032	0.752817	0.775869	0.793717	0.808901	0.835963	0.873838	0.902897	0.942404	0.971305
	0.06	0.692958	0.729936	0.758829	0.783418	0.801732	0.817024	0.843453	0.861821	0.909597	0.94905	0.974459
	0.07	0.692958	0.733964	0.76681	0.79023	0.808863	0.824041	0.849896	0.867629	0.91827	0.95439	0.977979
	0.08	0.692958	0.735181	0.769283	0.793681	0.812758	0.829739	0.853691	0.871482	0.921053	0.955888	0.978036
	0.09	0.692958	0.741726	0.775823	0.803271	0.822711	0.838415	0.862253	0.882305	0.928982	0.964424	0.984929
	0.1	0.692958	0.750244	0.787071	0.81406	0.833553	0.850783	0.875987	0.894053	0.935604	0.966902	0.986128

Table S3. Finite element simulation results of hemi-spheroidal craters at $\Theta = \Theta_m$

$\hat{F}$		β													
		0.1	0.2	0.5	0.75	1	2	3	4	5	6	7	8	9	10
α	0.05	0	0	0	0	0	0	0	0	0	0	0.998221	1.00044	1.00046	1.00048
	0.1	0	0	0	0	0	0	0	1.00016	1.00088	0.999966	0.99889	0.99859	0.998395	0.984243
	0.15	0	0	0	0	0	0	1.00076	0.998293	0.995687	0.994494	0.994645	0.994912	0.995397	0.988369
	0.2	0	0	0	0	0	0.992795	0.995715	0.989758	0.988372	0.989014	0.989876	0.990879	0.991902	0.992504
	0.25	0	0	0	0	0	0.995473	0.984542	0.982515	0.984114	0.985966	0.987986	0.98915	0.990957	0.991867
	0.3	0	0	0	0	0.438962	0.984711	0.974122	0.974171	0.978028	0.981231	0.984133	0.98592	0.988219	0.989494
	0.35	0	0	0	0	0.908604	0.967335	0.961114	0.966533	0.972366	0.975974	0.979676	0.982842	0.984802	0.986444
	0.4	0	0	0	0.556324	0.953365	0.946933	0.950746	0.959501	0.966317	0.971782	0.976245	0.979174	0.981562	0.984322
	0.45	0	0	0	0.842755	0.960888	0.929603	0.941862	0.953605	0.962018	0.967674	0.972896	0.97633	0.979977	0.982255
	0.5	0	0	0	0.899637	0.949467	0.915365	0.934915	0.948405	0.958394	0.966047	0.970984	0.976018	0.979124	0.981675
	0.55	0	0	0.224251	0.921537	0.928363	0.901343	0.92533	0.941595	0.953267	0.960702	0.967723	0.97207	0.975557	0.978408
	0.6	0	0	0.574303	0.914403	0.899265	0.889021	0.918586	0.936739	0.949407	0.957642	0.96497	0.96975	0.973567	0.976685
	0.65	0	0	0.726073	0.898018	0.86054	0.878106	0.911171	0.931433	0.945352	0.954359	0.962324	0.967516	0.972924	0.976282
	0.7	0	0	0.774089	0.869442	0.818763	0.867966	0.905291	0.927567	0.9428	0.954033	0.961219	0.966773	0.972754	0.976338
	0.75	0	0	0.803562	0.827854	0.786113	0.857902	0.899034	0.923094	0.937893	0.949755	0.957472	0.963419	0.969599	0.973431
	0.8	0	0	0.80051	0.779013	0.7613	0.848247	0.892921	0.918705	0.934482	0.947085	0.955266	0.963122	0.968106	0.972159
	0.85	0	0	0.786716	0.722447	0.743072	0.839745	0.887773	0.915216	0.933618	0.945266	0.955643	0.962241	0.967477	0.971733
	0.9	0	0	0.748796	0.685597	0.724747	0.833695	0.882989	0.911989	0.931403	0.943614	0.954578	0.961482	0.966956	0.971403
	0.95	0	0	0.707101	0.658813	0.708784	0.82518	0.877227	0.907616	0.927874	0.940656	0.952028	0.959244	0.964962	0.969603
	1	0	0	0.653268	0.637126	0.69272	0.818424	0.872442	0.903924	0.923054	0.939446	0.949243	0.956766	0.962724	0.967559